BRAIN CONNECTIVITY
Volume 3, Number 5, 2013

DOI: 10.1089/brain.2013.0157

Identifying Functional Networks Using Endogenous Connectivity in Gamma Band Electrocorticography

Andrew L. Ko,[1,2] Kurt E. Weaver,[3] Shahin Hakimian,[4] and Jeffrey G. Ojemann[5]

Abstract

Correlations in spontaneous, infra-slow (< 0.1 Hz) fluctuations in gamma band (70–100 Hz) signal recorded using electrocorticography (ECoG) reflect the functional organization of the brain, appearing in auditory and visual sensory cortex, motor cortex, and the default mode network (DMN). We have developed a data-driven method using co-modulation in spontaneous, infra-slow, and gamma band power fluctuations in ECoG to characterize the connectivity between cortical areas. A graph spectral clustering algorithm was used to identify networks that appear consistently. These networks were compared with clinical mapping results obtained using electrocortical stimulation (ECS). We identify networks corresponding to motor and visual cortex with good specificity. Anatomic and functional evidence indicates that other networks, such as the DMN, are also identified by this algorithm. These results indicate that it may be possible to map functional cortex using only spontaneous ECoG recordings. In addition, they support the hypothesis that infra-slow co-modulations of gamma band power represent the neurophysiological basis underlying resting-state networks. Methods examining infra-slow co-modulations in gamma band power will be useful for studying changes in brain connectivity in differing behavioral contexts. Our observations can be made in the absence of observable behavior, suggesting that the electrical mapping of functional cortex is feasible without the use of ECS or task-mediated evoked responses.

Key words: default mode network; endogenous connectivity; functional networks; gamma band; infra-slow fluctuations; spontaneous ECoG

Introduction

Evolving technology and analytical approaches in neuroscience have led to a greater emphasis on large-scale, inter-connected networks as a key architecture for orchestrating cognitive and sensorimotor function. Such connectivity is evident even in the spontaneous activity of the brain, and it has been seen using modalities such as resting-state functional magnetic resonance imaging (rsfMRI), electroencephalography (EEG), magnetoencephalography (MEG), and electrocorticography (ECoG). In this study, spontaneous ECoG is used in a data-driven fashion to identify functional networks. Our approach clusters electrodes based on co-fluctuations in high-gamma (HG; 70–100 Hz) power within a given time period and iterates this process over multiple segments to determine how consistently electrodes appear in the same cluster across time. This metric is called clustering stability, and it is used to derive stable, functionally connected networks. We call this analysis infra-slow clustering (ISC). It identifies electrodes overlying functional cortical fields corresponding to motor, visual, and default mode network (DMN) cortex. These networks show functional relationships that are consistent with rsfMRI studies of resting-state networks. ISC provides a method for analyzing endogenous connectivity between brain regions in the resting state, and it can be useful for analyzing temporal dynamics of these interactions in differing behavioral or attentional states.

It has become increasingly clear that general cognitive and sensorimotor functions emerge as a dynamic interplay between functionally connected but spatially distributed cortical regions, and these are evident even in the spontaneous activity of the brain. Providing a primary role in this shift are innovations in the imaging modalities, specifically within rsfMRI and corresponding computational estimates of functional connectivity (fc), which plot voxel-wise correlations of infra-slow (< 0.1 Hz) blood oxygenation level-dependent

[1]Department of Neurological Surgery, University of Washington, Seattle, Washington.
[2]Department of Neurological Surgery, Oregon Health Sciences University, Portland, Oregon.
[3]Department of Radiology, Integrated Brain Imaging Center, University of Washington, Seattle, Washington.
[4]Department of Neurology, University of Washington, Seattle, Washington.
[5]Department of Neurological Surgery, Seattle Children's Hospital, Seattle, Washington.

(BOLD) signal fluctuations extracted during a resting period (Kelly et al., 2012). Through studies of fc, it has become evident that general cognitive and sensorimotor function emerge as a dynamic interplay between functionally connected, but spatially distributed cortical regions, in which segregated cortical hubs contribute a specialized component to the overall global function (Deco et al., 2011). More recent studies, however, have observed experimentally induced BOLD shifts and modulations between discrete networks, proposing the notion that adaptive and flexible function is facilitated through the dynamic interaction across multiple systems (Bassett et al., 2011; Bianciardi et al., 2009).

Despite being an intuitively plausible mechanism underlying the application of rsfMRI, fc BOLD measurements are rooted in a complex physiological pathway linking neural activity to cerebrovascular changes. As a consequence, numerous non-neural "noise" has been shown to alter patterns of fc (Power et al., 2012). Scalp-based electrophysiological (e.g., EEG and MEG) studies, which are less susceptible to cerebrovascular noise, have attempted to reconcile such discrepancies by combining resting-state periods with, for example, large-scale coherence measurements (Murias et al., 2007). However, scalp-based recordings provide poor resolution of deep cerebral structures and low signal to noise within the HG (e.g., 75–200 Hz) range, a band of activity that most strongly reflects evoked cortical activity (Jerbi et al., 2009). Other efforts have used invasive, sub-dural recordings typically done for clinical mapping of epileptic foci. Such ECoG recordings are extracted directly from the cortical surface and allow for a very high signal-to-noise ratio within the HG range (Crone et al., 1998). Increases in HG band power have been shown to reflect local cortical function (Crone et al., 1998; Miller et al., 2009), and, accordingly, ECoG has been used to characterize the neurophysiological basis of the rsfMRI resting state fc phenomenon. Results from several studies converge on the hypothesis that spontaneous, infra-slow co-fluctuations (< 0.1 Hz) in HG band power appear to reflect the functional organization of various, known cortical fields. This observation has been noted within the auditory and visual sensory cortex (Leopold and Logothetis, 2003; Nir et al., 2008), motor cortex (He et al., 2008) as well as the DMN (Ko et al., 2011).

These studies suggest that functional cortical fields may be mapped using spontaneous, infra-slow co-modulations of HG power in ECoG. Analogous studies mapping sensorimotor cortex using spontaneous signal at infra-slow time scales are proposed in the fMRI and ECoG literature (Breshears et al., 2012; Zhang et al., 2009). In the current study, we use a graph spectral clustering algorithm to simultaneously identify several functional networks exhibiting correlations in infra-slow (< 0.1 Hz) fluctuations in HG (70–100 Hz) band-limited power (BLP). This method is distinct from those measuring slow cortical potentials (< 0.5 Hz) directly (Breshears et al., 2012). We compared clusters identified with ISC to functional maps derived from electrocortical stimulation (ECS), the gold standard for the clinical identification of motor and visual systems, and found that this algorithm is highly specific. Additional functional networks thus identified appear anatomically consistent with relevant large-scale networks such as the DMN. Finally, the functional relationships between networks appear consistent with those determined using fMRI, exhibiting anti-correlated activity as seen in other studies (Fox et al., 2006). Our results indicate that infra-slow spontaneous modulations in HG ECoG signal can be used to identify functional networks, support the notion that modulations in HG power represent an electrophysiological correlate to the BOLD fluctuations used to characterize resting-state networks, and may be useful in the study of functional relationships between these cortical regions over time and between behavioral contexts. Our observations can be made in the absence of observable behavior and persist in asleep patients (Breshears et al., 2010), implying that the electrical mapping of functional cortex may be possible without the use of ECS or task-based evoked responses. This would be particularly useful in peri-operative mapping for resection of seizure foci or tumors near eloquent cortex, when an awake craniotomy may not be feasible.

Materials and Methods

Subjects

Subjects were selected from patients undergoing invasive sub-dural electrode monitoring for seizure localization at Seattle Children's Hospital and Harborview Medical Center (Seattle, WA). Recordings from four children and four adults were screened for use. These subjects were selected, because they possessed long, spontaneous ECoG recordings that had been pre-processed as described in a previous study (Ko et al., 2011). One subject was eliminated from analysis due to excessive artifact over motor cortex electrodes during clinical monitoring. One subject was excluded, as the pre-processed data did not include electrode coverage of motor cortex, leaving three children and three adult subjects for clustering analysis. Demographic and clinical data are included in Table 1. All data gathering was done in accordance with protocols approved by the Institutional Review Board at Seattle Children's Hospital and the University of Washington.

ECoG acquisition, cortical mapping, and electrode localization

Sub-dural platinum electrode arrays and strips (Ad-Tech, Racine, WI) with 2.3 mm diameter exposed and 10 mm inter-electrode distance were implanted. Data were acquired using standard XLTEK (Oakville, Canada) clinical system parameters. These impose a high-pass filter on AC-coupled data at about 0.1 Hz. Sampling rates ranged from 250 to 2000 Hz. Data were gathered over a long period (6–23 h) of time, and contiguous seizure- and artifact-free segments were identified. Segments recorded during awake behavior restricted to the hospital bed were used for analysis. Periods during which patients appeared to be asleep as determined by video monitoring were excluded, as polysomnography was not available for accurate sleep staging. For each subject, more than 18,000 sec of data were analyzed.

A cortical mapping of motor areas was performed using standard clinical protocols. Briefly, motor responses were elicited with pair-wise stimulation of electrodes with high-frequency (50 Hz), alternating polarity square pulses lasting 2–5 sec, starting at an intensity of 1–2 mA and progressing until 10 mA was reached or after discharges were noted.

Surface electrode positions were localized using the Location on Cortex (LOC) package (Miller et al., 2007) from anterior-

Table 1. Subject and Clustering Data

Subject	S1		S2		S3		S4		S5		S6	
Age/sex	11/F		11/F		7/F		24/M		43/F		20/F	
Sampling rate (Hz)	500		500		500		250		2000		500	
Electrode number	118		98		94		126		116		126	
Mapping modality	ECS	ISC	ECS	ISC	ECS	ISC	ECS	ISC	ECS	ISC	ECS	ISC
Hand motor electrode	G44				G55	G55		G12	G11		G6	
	G45	G45			G56	G56	G13		G19		G7	G7
	G46	G46				G62	G14		G20	G20	G13	
		G47			G63	G63	G20	G20	G26	G26	G14	G14
	G53	G53			G64	G64	G21		G27	G27	G15	G15
	G54	G54					G22		G28	G28		G16
	G55	G55					G28	G28		G33	G21	
	G56						G29	G29	G35	G35	G22	G22
	G61	G61					G30		G36	G36	G23	G23
	G62	G62					G31					
		G64					RMF13					
		MFP4					RMF14	RMF14				
		MFP5					RMF15	RMF15				
							RIMP7	RIMP7				
							RIMP8	RIMP8				
Leg motor	MFP4						RSMP7		G2			
	MFP5						RSMP8		G3	G3		
	MFP12	MFP12					RSMP15	RSMP15	G10	G10		
	MFP13	MFP13					RSMP16	RSMP16	G11			
Face motor				G37		G23					G29	
				G38		G24					G30	
			G45	G45	G30						G36	
				G46	G32						G37	G37
			G53	G53	G38	G38					G38	
			G54	G54	G40						G44	
			G62		G47	G47					G45	G45
					G48	G48					G46	G46
											G52	
											G53	
												RAF 3
												RAF 4
Visual electrodes							RIMP1	RIMP1				
							RIMP2	RIMP2				
							RIMP9	RIMP9				
							RIMP10	RIMP10				

	True	False	
Positive	53	13	66
Negative	584	28	612
Totals	637	41	678
Sensitivity	0.65	PPV	0.80
Specificity	0.98	NPV	0.96

Demographic data for subjects are presented here. In addition, electrodes identified as motor and visual system mapping using ECS or ISC are presented for comparison.

G, grid; LAI, left anterior interhemispheric; MFP, medial frontal-parietal; RMP, right medial parietal; RSMP, right superior medial parietal; RIMP, right inferior medial parietal; ECS, electrocortical stimulation; ISC, infra-slow clustering.

posterior and lateral skull X-rays. In pediatric patients, electrodes were localized from high-resolution postimplantation CT scans using the Bioimage Suite (Papademetris et al., 2006).

Anatomic localization of resting-state networks with anti-correlated activity was performed using fMRI seed locations described in previous studies (Fox et al., 2005, 2006). These sites are delineated in Table 2.

ECoG analysis and spectral clustering

The use of spontaneous HG power fluctuations has been established in other studies of connectivity, and allows an examination of arbitrarily low frequencies that are not otherwise accessible due to the high-pass filter used in most clinical recording systems (He et al., 2008; Ko et al., 2011; Nir et al.,

Table 2. Talairach Coordinates of Anti-Correlated Resting-State Networks

	Brodmann's area	*Anatomic name*	*Side*	*Talairach coordinates*
Task negative network	31	pCC	M	(−2, −36, 37)
	19	LP	L	(−47, −67, 36)
			R	(53, −67, 36)
	32/10	MPFC	L	(−3, 39, −2)
			R	(1, 54, 21)
Task positive network	7	IPS	L	(−23, −66, 46)
			R	(25, −58, 52)
	7/40	iPL	L	(−42, −44, 49)
			R	(47, −37, 52)
	6	FEF	L	(−24, −12, 61)
			R	(28, −7, 54)
	6/32	SMA	M	(−2, 1, 51)
	46	DLPFC	L	(−40, 39, 26)
			R	(38, 41, 22)
	19	MT	L	(−47, −69, −3)
			R	(54, −63, −8)

pCC, posterior cingulate cortex; LP, lateral parietal; MPFC, medial prefrontal cortex; IPS, inferior parietal sulcus; iPL, inferior parietal lobule; FEF, frontal eye fields; SMA, supplementary motor area; DLPFC, dorsolateral prefrontal cortex; MT, middle temporal gyrus; M, medial; L, left; R, right.

2008). In addition, correlations in the infra-slow component of BLP have been shown to be more specific to the functionally related cortex (Nir et al., 2008). Our approach employs clustering of electrodes based on co-fluctuations in HG power within a given time segment and iterating this over multiple segments to produce a similarity matrix reflecting how consistently electrodes appear in the same cluster across segments. Our hypothesis is that the composition of clusters during individual segments might change (as correlations between electrode time-series change over time), but that consistent networks would emerge over a large enough number of time segments. This is because the clinical recordings used may not reflect a true "resting state," as patients are awake and without any controls imposed on their behavioral state. Shorter-term changes in correlations between electrodes could represent behaviorally mediated interactions between networks. However, over enough time, a "resting state" configuration should be more consistent than dynamic configurations associated with specific activities.

ECoG voltage signals were re-referenced to the common average. Spectral power time series were generated by computing the fast-Fourier transform after application of a Hanning window to nonoverlapping segments. Segment length was chosen to give a 2 Hz frequency resolution at a sampling rate of 2 Hz, where $v(t)_i$ is the time-dependent ECoG voltage from electrode i,

$$P(f,t)_i = |FFT[v(t)_i]|^2 \tag{1}$$

is a time-series representation of the average power of each Fourier component of the voltage during each 0.5 sec segment. The HG BLP was generated by averaging $P(f, t)_i$ for $f = 70$–100 *Hz*. This approach to generating gamma BLP has been previously described (Ko et al., 2011).

Inter-electrode correlations specific to functional cortical fields are more pronounced at infra-slow frequencies (Nir et al., 2008). We, therefore, low-pass filtered our HG power time series using a finite impulse response filter (length 100 sec) to isolate the infra-slow (< 0.1 Hz) fluctuations. This time series is denoted $x(t)_i$ for each electrode i. Correlation coefficients between each time series were generated using nonoverlapping, 300-sec segments of $x(t)$ with a total number of segments denoted *segn*. This choice of segment length was chosen to be commensurate with the time scales used in the acquisition of rsfMRI, and, in part, to provide a sufficient number of samples for use in the clustering analysis, and it has been used in previous studies (Ko et al., 2011; Nir et al., 2008).

For a given segment, for electrodes i and j,

$$\rho_{i,j} = \frac{cov(x(t)_i, x(t)_j)}{std(x(t)_i) \times std(x(t)_j)} \tag{2}$$

gives the Pearson correlation coefficient. Significant correlations were determined by a comparison to surrogate data generated by time shifting $x(t)_i$ by a random time lag for each electrode. This lag was longer than the segment length and shorter than the total length of the signal. This preserves auto-correlations while destroying correlations between electrode time series. Surrogate correlations were calculated as described earlier for 2000 surrogate time series. Significant correlations were selected using a False Discovery Rate (FDR) $q = 0.025$ in a two-tailed fashion, identifying significant positive as well as negative correlations. Only positive correlations were used for clustering.

In principle, any of several clustering algorithms might be effective. We chose a normalized spectral clustering algorithm as described by Shi and Malik (2000) and von Luxburg (2007). A schematic of the algorithm is shown in Figure 1. Given a vertex set $E = \{e_1, \ldots e_n\}$, where n is the number of electrodes, a weighted adjacency graph

$$G_s = ([r_{i,j}]_{i,j=1:n}),$$

where

$$r_{i,j} = \begin{cases} \rho_{i,j}, & \textit{if positive and significant} \\ 0, & \textit{otherwise} \end{cases} \tag{3}$$

was created using significant correlations for each segment $s = 1 \ldots segn$. Several methods for determining neighborhood size exist; we chose a mutual k-nearest-neighbors graph that was constructed with $k_{nn} = 2$. This was determined empirically as a good balance between generating trivial clusters containing one or two electrodes ($k_{nn} = 3$), and one or two very large clusters ($k_{nn} = 1$). The nearest-neighbors graph,

$$W = ([w_{i,j}]_{i,j=1:n})$$

where

$$w_{i,j} = \begin{cases} r_{i,j} & \textit{if neighbors} \\ 0, & \textit{otherwise} \end{cases} \tag{4}$$

has vertices $e_i \in E$ of degree $d_i = \sum_{j=1}^{n} w_{ij}$. The matrix D is defined with $d_{1\ldots n}$ on the diagonal. The graph Laplacian is $L = D - W$, which was used to solve the generalized eigenproblem $Lv = \lambda Dv$.

The gap heuristic (von Luxburg, 2007) was used to select an ideal number of clusters to identify denoted K. The eigennumbers λ were examined, and the number of clusters was

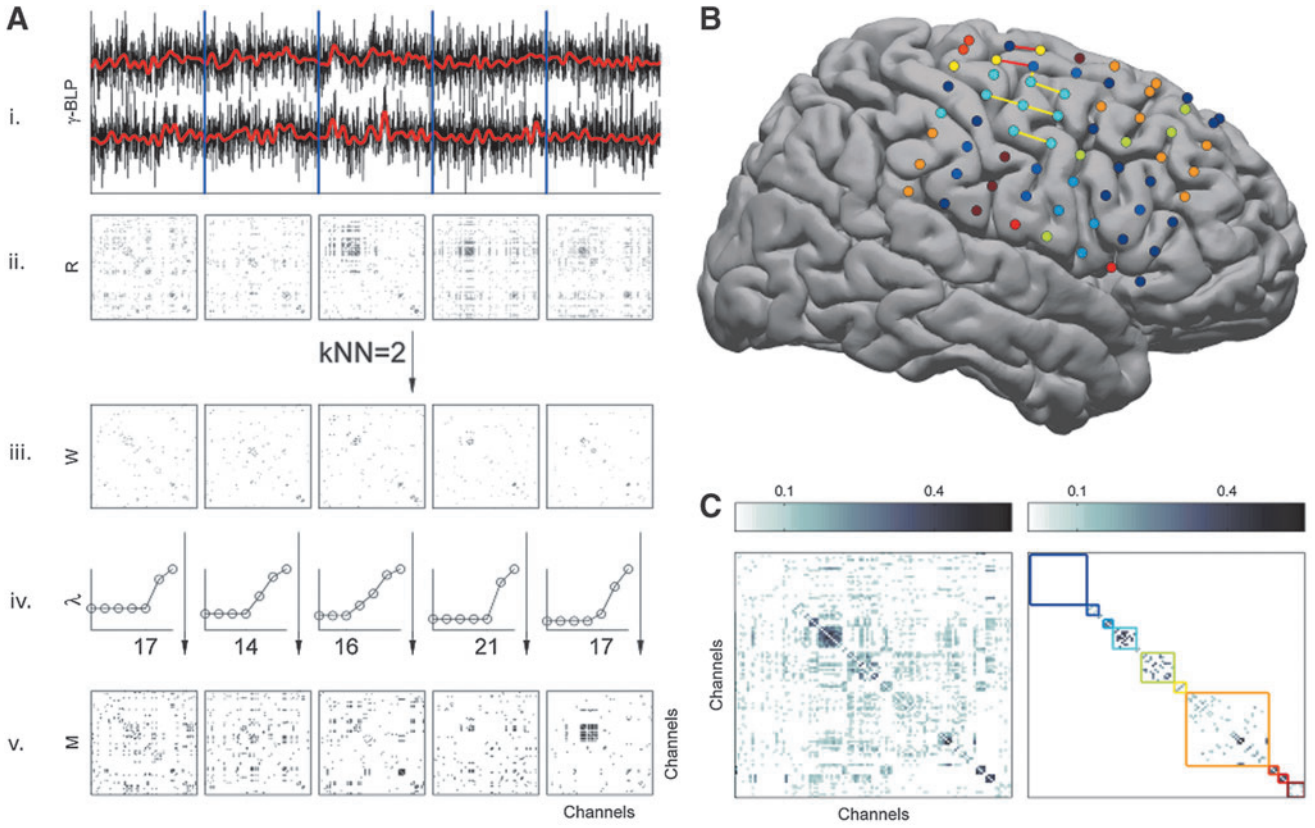

FIG. 1. Infra-slow spectral clustering algorithm. **(A) i,** Gamma band-limited power (BLP) is low-pass filtered at <0.1 Hz (red). Nonoverlapping, 300 sec segments are created (blue dividing lines) **ii,** Correlation coefficients for each segment between all electrodes are compared with surrogate time series, and significant interactions between channels are represented in a matrix here denoted R. **iii,** This is converted to a mutual nearest-neighbor adjacency matrix W with the number of neighbors ($k_{nn}=2$). **iv,** The normalized spectral clustering algorithm is applied as described in the "Materials and Methods" section. An abbreviated plot of generated eigennumbers illustrates the "gap heuristic" used to select the number of clusters used, and the *k*-means algorithm is used to identify electrode clusters (on *x*-axis). **v,** An adjacency matrix denoted M is used to represent clustering of electrodes for one time segment. **(B)** A cumulative sum of M across all segments is used to generate a final clustering as shown for subject S5. Electrocortical stimulation (ECS) mapping of hand (yellow lines) and leg (red lines) motor areas is shown on this template brain, along with clusters that correspond (light blue, yellow electrodes). **(C)** Left: The cumulative sum of M values over time that is used for the final clustering. Right: The nearest-neighbors matrix used for final clustering. The algorithm results are denoted with each cluster represented by a colored rectangle corresponding to the electrode colors in **(C)**.

chosen when the differential between consecutive eigennumbers exhibits a "gap," where

$$\lambda > 0 \; and \; \Delta(\lambda_{i,i+1})_{i=1\ldots n-1} > \frac{1}{2}\sigma\lambda. \tag{5}$$

The matrix $\Upsilon \in \mathbb{R}^{n\times K}$ was then defined with the eigenvectors $v_1 \ldots v_K$ as columns, with vectors y_i corresponding to the rows of matrix Υ. The *k*-means algorithm was used to cluster each $(y_i)_{i=1\ldots n}$ into clusters $c_1 \ldots c_K$.

This process was iterated across all segments to create the matrix

$$M^{n\times n\times segn} = [u_{i,j,s}]_{i,j=1\ldots n;s=1\ldots segn}$$
$$u_{i,j,s} = \begin{cases} 1, if \; e_i \; and \; e_j \; are \; in \; same \; cluster \; for \; segment \; s \\ 0, if \; otherwise \end{cases} \tag{6}$$

and across multiple segments,

$$\mathrm{M}^{sum} = \textstyle\sum_{s=1}^{segn}([M_{i,j,s}])_{i,j=1\ldots n} \tag{7}$$

This matrix reflects what we call clustering stability, and was normalized to the unit scale. It is a measure of how often a given electrode pair clusters together over all time segments. If electrodes *i* and *j* were to cluster together across every segment, $\mathrm{M}^{sum}{}_{i,j}=1$, and if they never cluster together, $\mathrm{M}^{sum}{}_{i,j}=0$. A similarity graph is constructed using values of M^{sum} (Fig. 1C, right). The spectral clustering algorithm is applied as described earlier to give a final clustering $C_0 \ldots C_K$, where singleton clusters are grouped into C_0.

Data analyses

As is obvious from Figure 1C, there is variation as to how often a given electrode pair clusters with other electrodes. While M^{sum} (Eq. 7) represents clustering stability integrated over the entire signal, the matrix M (Eq. 6) represents the clustering relationship between each electrode pair during each time segment, and it can be used to examine spatial relationships. At any given time *t*, a certain percentage of electrode

pairs have clustered together; if one examines a constant group of electrodes over time, values of M can be used to give an estimate of the spatial stability of that cluster over the entire signal; in other words, the percentage of a given cluster of electrodes that is present during a given time segment can be calculated using these values, and displayed as a function of time. Within-cluster averages of significant correlation in infra-slow HG power between groups of electrodes can be examined similarly, along with standard error of the means. Statistical significance was determined via bootstrapping in which electrode identities were shuffled before calculation of these within-cluster statistics. *p*-Values were calculated using 2000 bootstrap samples, and significance levels were set for an FDR of $q = 0.05$.

The functional relationship between clusters was also analyzed by examining anti-correlations. Given the matrix of significant correlations (including negative correlations)

$$R^{sig} = ([r_{i,j}]_{i,j=1:n})_{s=1\ldots segn} \tag{8}$$

and the final clustering $C_0 \ldots C_K$, let R_c^{sig} represent a rearrangement by cluster. For a given cluster k,

$$R_{c_k}^{sig} = ([r_{x,y}]_{x=c_k, y=1\ldots n})_{s=1\ldots segn} \tag{9}$$

gives all significant interactions within itself and with other clusters. This can be consolidated into a single number that is normalized for cluster size

$$NR_{c_k} = \frac{\#\ of\ R_{c_k}^{sig} < 0}{total\ \#\ of\ R_{c_k}^{sig}} \tag{10}$$

and provides a measure of anti-correlation between clusters. Bootstrapping by shuffling electrode identity as described earlier (2000 samples) identifies clusters with a significantly higher proportion of negative correlations between their electrode pairs (FDR = 0.05).

The reliability of the algorithm was evaluated by generating "sub-clustered" networks, essentially resampling the clustering in a jackknife-like process. Each sample starts with the signal at some time t, representing a 300-sec segment, and the clustering process is iterated over a number of segments ($segn_{sub} = 20$) less than the total signal. For a given starting point,

$$M_t^{sub} = \sum_{s=t}^{t+segn} [u_{i,j,s}]_{i,j=1\ldots n} \tag{11}$$

is analogous to M^{sum} for the entire signal. The sub-clustering is repeated by sliding this 20-segment window across the entire signal for each subject for a total number of iterations *nsub*. A normalized two-dimensional correlation was used to evaluate the similarity between each value of M_t^{sub} and M^{sum}, giving a measure of how well sub-clustering correlates with the final clustering at each time point. In addition, this resampling of networks can be used to determine how quickly the clustering algorithm derives a stable series of networks, using the correlation between M_{t-1}^{sub} and M_{t+1}^{sub} (Fig. 1D), with the repeated iterations giving an estimate of variation over the course of the signal.

Results

ISC identifies functional networks

ECS mapping was used to identify functional cortical areas; our clinical data included results for motor function in all subjects, and visual cortex and language mapping in one subject each. In each of six subjects, spectral clustering of correlations in infra-slow gamma band power fluctuations produced networks corresponding to motor cortex as identified using cortical stimulation mapping (Fig. 2). Interestingly, our algorithm provided somatotopic specificity, identifying hand versus leg versus face motor cortex. Other functional networks were identified as well. In one subject, visual cortex was mapped during seizure monitoring, and a corresponding cluster of electrodes was identified by our algorithm (Fig. 2A). In one subject with bilateral electrode coverage, the face motor cluster identified using ISC included electrodes on the side contralateral to but consistent with ECS mapping of facial motor areas (Fig. 2B). This shows that our algorithm identifies long-distance and inter-hemispheric interactions.

Overall, this algorithm identified a total of 64 sensorimotor or visual electrodes with 53 true positives. The sensitivity of this approach is only about 65%. However, the specificity of our clustering was quite good at 98%, with a negative predictive value of 95% (Table 1).

ISC networks exhibit large-scale anti-correlated behavior

Our algorithm also detects attentional networks related to and including the DMN. Three subjects (S1, S4, S6) possessed electrode coverage of the posterior cingulate cortex, an anatomic region consistently identified as belonging to the DMN (Damoiseaux et al., 2006; Fox et al., 2005), and our algorithm identified a cluster overlying this region in each of these subjects (Fig. 3). Furthermore, these clusters exhibited functional relationships to cortical areas consistent with task-positive regions as reported in the fMRI literature (Fox et al., 2005, 2006). Those regions with infra-slow gamma band activity that are negatively correlated with the DMN cluster correspond to seed regions identified with attentional systems in the rsfMRI literature, including the frontal eye fields (FEF), inferior parietal lobule (iPL), and dorsolateral prefrontal cortex (DLPFC) in particular (Fig. 3). The Talairach coordinates for these regions are listed in Table 2. In contrast, the DMN regions do not exhibit significantly anti-correlated activity with the motor or visual clusters (Fig. 3). This result mirrors the large-scale architecture seen in rsfMRI (Fox et al., 2006).

fc varies over time

Over all subjects, the significant positive correlations within a cluster, $\bar{\rho}_{in}$ are higher than significant positive correlations between electrodes in different clusters, $\bar{\rho}_{out}$ (Fig. 4B). This holds across all subjects and is statistically significant by Student's *t*-test ($S1: \bar{\rho}_{in}/\bar{\rho}_{out} = 0.41/0.31$; $S2: \bar{\rho}_{in}/\bar{\rho}_{out} = 0.42/0.33$; $S3: \bar{\rho}_{in}/\bar{\rho}_{out} = 0.37/0.33$; $S4: \bar{\rho}_{in}/\bar{\rho}_{out} = 0.41/0.33$; $S5: \bar{\rho}_{in}/\bar{\rho}_{out} = 0.34/0.30$; $S6: \bar{\rho}_{in}/\bar{\rho}_{out} = 0.34/0.32$; all $p < 0.0001$). The average significant correlation in a cluster appears to vary from cluster to cluster, and, in some cases, is below the average significant correlation between nonclustered, singleton electrodes (Fig. 4B). This is not surprising, as the algorithm uses the measure of cluster stability M to construct clusters rather than only correlation values; since we use a mutual nearest-neighbors graph as a similarity measure, singleton electrodes may be significantly correlated with other electrodes that have other, more strongly correlated interactions. On the other hand, some electrode pairs may have lower correlation values but still consistently sub-cluster together.

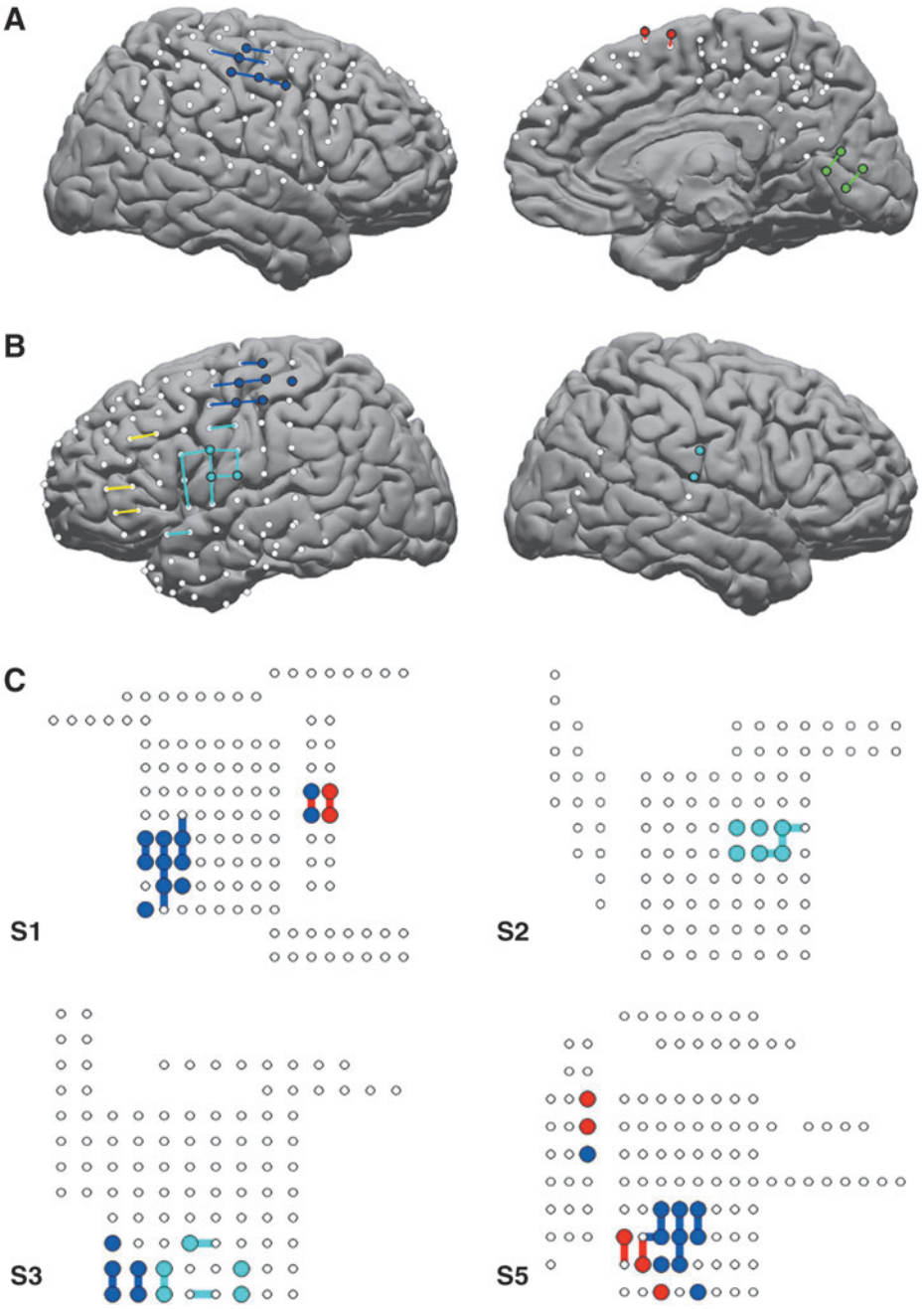

FIG. 2. Spectral clustering identifies clusters corresponding to motor and visual cortex mapped using ECS. ECS results are denoted with colored lines as follows: blue for hand motor, cyan for face motor, red for leg motor, and green for visual cortex. Clusters derived from the infra-slow clustering (ISC) algorithm are denoted in corresponding electrode colors. **(A)** Results for subject S4 show a cluster of electrodes (blue electrodes) that is spatially consistent with ECS mapping of hand motor cortex (blue lines). Clusters corresponding to ECS mapping of leg motor (red electrodes, red lines) and visual cortex (green electrodes, green lines) are shown on the right. **(B)** ISC identifies bilateral face motor cortex in subject S6. Note that ECS testing was not performed on the right side, but the location of the ISC cluster is anatomically consistent across both hemispheres. **(C)** Schematic representation of electrodes with ISC and ECS mapping shown for the remaining subjects shows that each subject has an ISC-identified cluster that corresponds spatially with the ECS maps.

Similar to correlation, the cluster stability measure is higher for clusters compared with noncluster electrodes, and exhibits greater variation over time compared with correlation values (Fig. 4C, D). Motor clusters tend to have a higher within-cluster stability, with an average across subjects of 0.44 (range: 0.32–0.52, SD: 0.062) compared with 0.37 (range: 0.19–0.59, std: 0.077) for nonmotor clusters ($p = 0.005$ by Student's t-test). The variation in average stability across clusters is surprising, with some clusters having very low stability values. For example, for subject S5, average cluster stability can be as low as 0.2 for several clusters (Fig. 4C, right).

Two factors would appear to contribute to the variation in clustering stability: Electrodes may variably sub-cluster with other functional networks over time, and a given electrode may not have significant interactions with any other electrode for some segments, reflecting heterogeneity in electrode–electrode interactions over time. In other words, the sub-clustering results for any one given time segment does not necessarily resemble the final clustering over the whole signal.

Stable clusters emerge over time

However, despite the variation in cluster stability, the results of this algorithm over a long period of time appear reliable. We examined this in two ways, using multiple subsets of the signal analyzed, calculating M_t^{sub} (Eq. 11) for these subsets. M_t^{sub} begins to resemble itself relatively quickly, with a normalized two-dimensional cross-correlation of more than 98% within six 300-sec segments (Fig. 5A, B). After 1 h, the

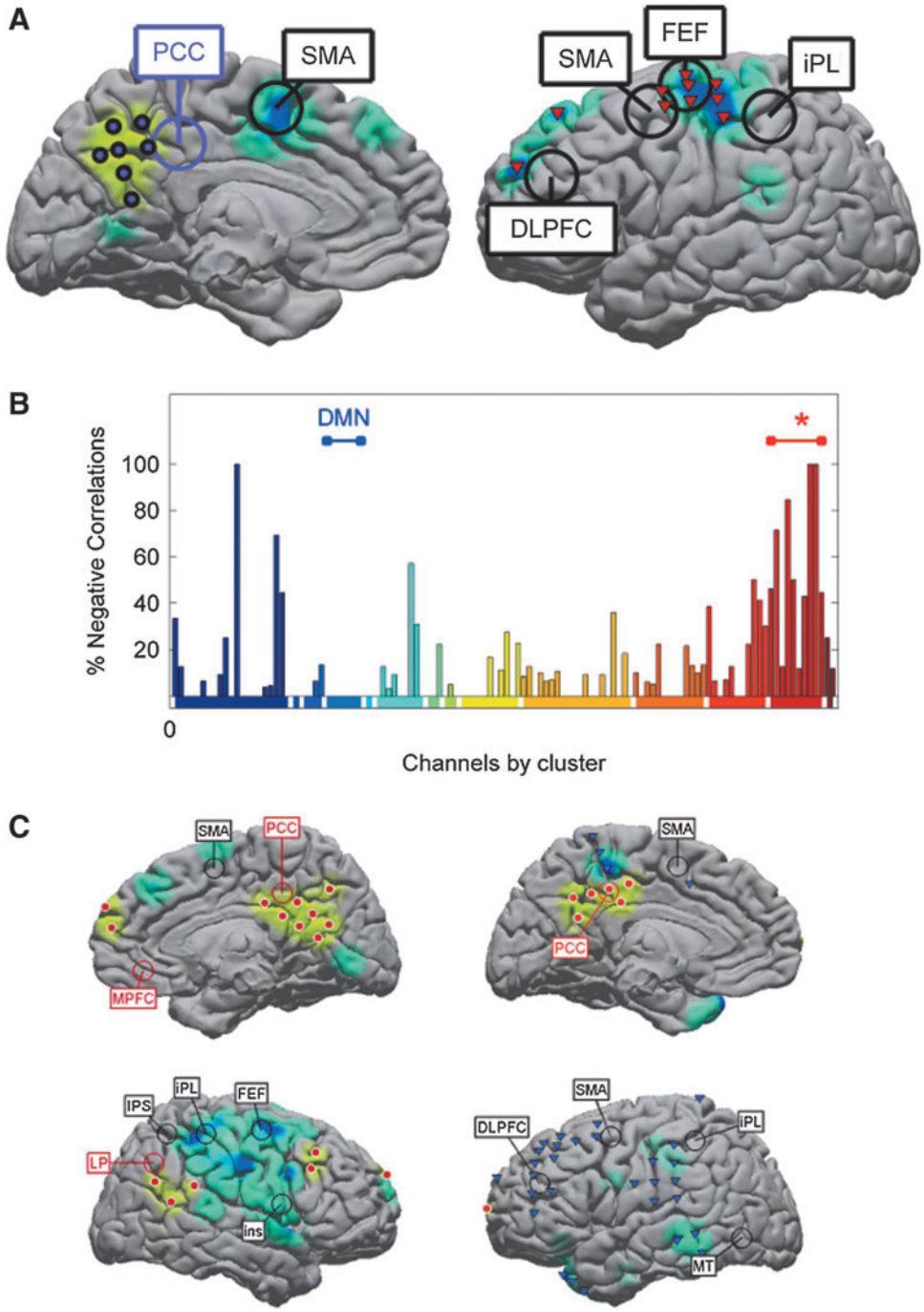

FIG. 3. ISC identifies clusters overlying putative default mode network (DMN) cortex, which show anti-correlated activity with dorsal attentional networks. **(A)** For subject S1, one ISC cluster overlies the posterior cingulate cortex (pCC), a region associated with the DMN in functional magnetic resonance imaging (fMRI) studies. Cortex underlying electrodes that have significant negatively correlated activity compared with those over the pCC are shaded blue. In addition, one ISC cluster, overlying the frontal eye fields (FEF), inferior parietal lobule (iPL), and dorsolateral prefrontal cortex (DLPFC), all areas shown to be anticorrelated with the pCC, is shown with inverted red triangles. Other electrodes are omitted for clarity. **(B)** The percentage of significant negative correlations between electrodes overlying DMN cortex and all other electrodes is shown, colored by clusters. The blue bar labels DMN electrodes; the red bar with asterisk indicates the cluster over FEF, iPL, and DLPFC shown in **(A)**. This cluster has a significantly higher proportion of negative correlations with the DMN than randomly generated networks ($p < 0.004$). **(C)** Left: Results of similar analyses with subject S4, showing extensive negatively correlated activity. DMN is indicated by yellow shading of cortex and red electrodes; anti-correlated areas are shaded in blue. The pCC and typically anti-correlated areas are labeled. Right: Again, one ISC cluster overlies pCC, and is significantly anti-correlated with a cluster (inverted purple triangles) that overlies anti-correlated fields derived from previous fMRI studies [iPL, middle temporal gyrus (MT), DLPFC].

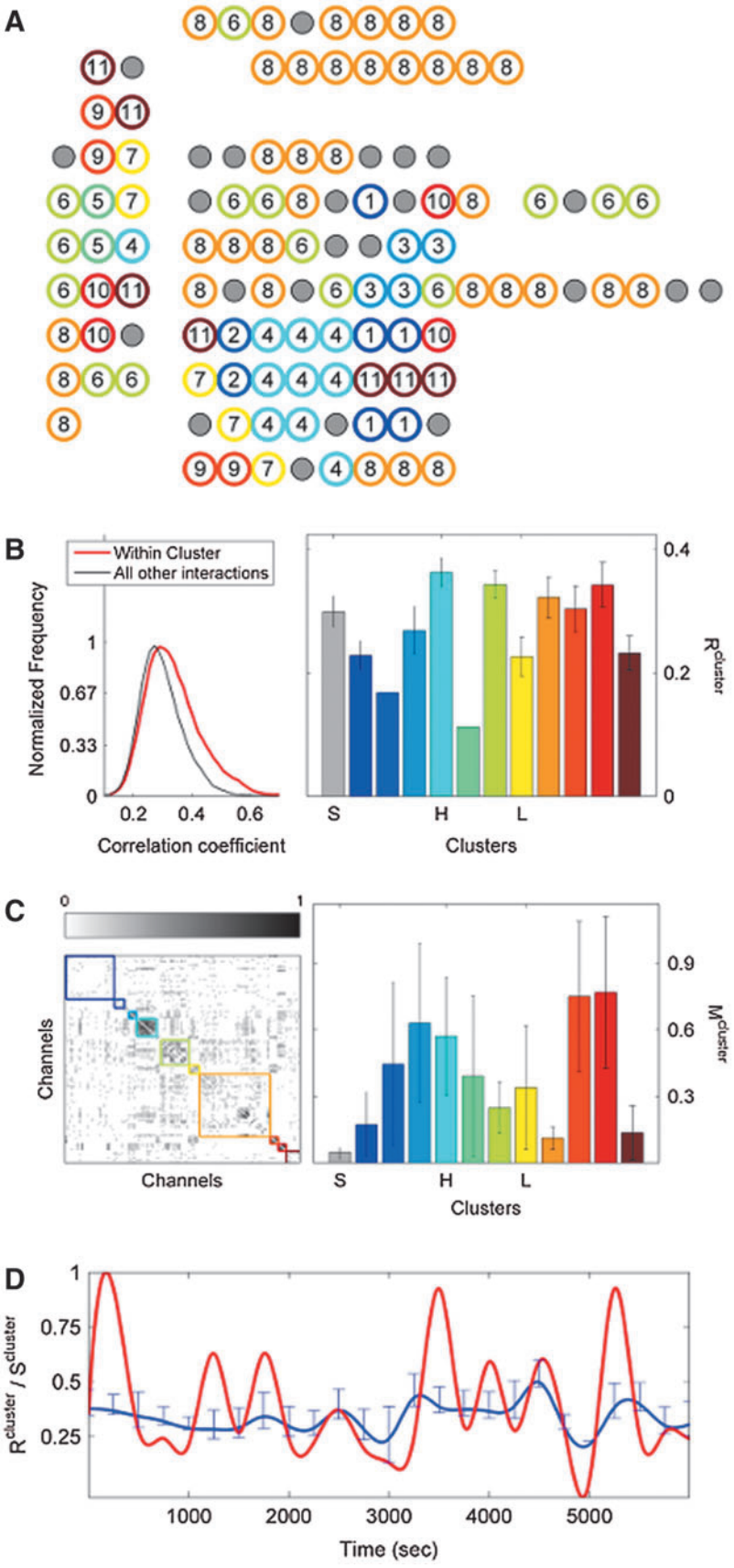

FIG. 4. Clustering over individual time segments varies significantly over the course of the signal. **(A)** Labeled schematic showing clustering results for subject S5. Clusters are numbered and also colored for identification. **(B)** Left: Histogram showing the significant correlation between electrodes within a single cluster (red line) and between electrodes in different clusters (black line) for the same subject. The difference in mean values is significant by Student's *t*-test (mean within: 0.34, mean between 0.3, $p < 0.001$). Right: The average significant correlation across time for each cluster is quite variable and can be very low. Singleton electrode interactions (gray) appear to be stronger than some clusters. **(C)** Left: The cumulative sum of cluster stability M over the entire signal is grouped by clusters as indicated by colored rectangles. Note that this matrix shows that electrodes often seem to sub-cluster with electrodes outside the final clustering. In addition, not all electrode interactions within a cluster are present throughout the entire signal. These two factors contribute to the high variation in cluster stability, as seen on the right, where the average $M_k^{cluster}$ for each cluster is shown with error bars denoting standard deviation. **(D)** The average significant correlation and cluster stability for the hand motor cluster (denoted H, light blue) is shown over 6000 sec. A small change in average correlation creates a large change in cluster stability.

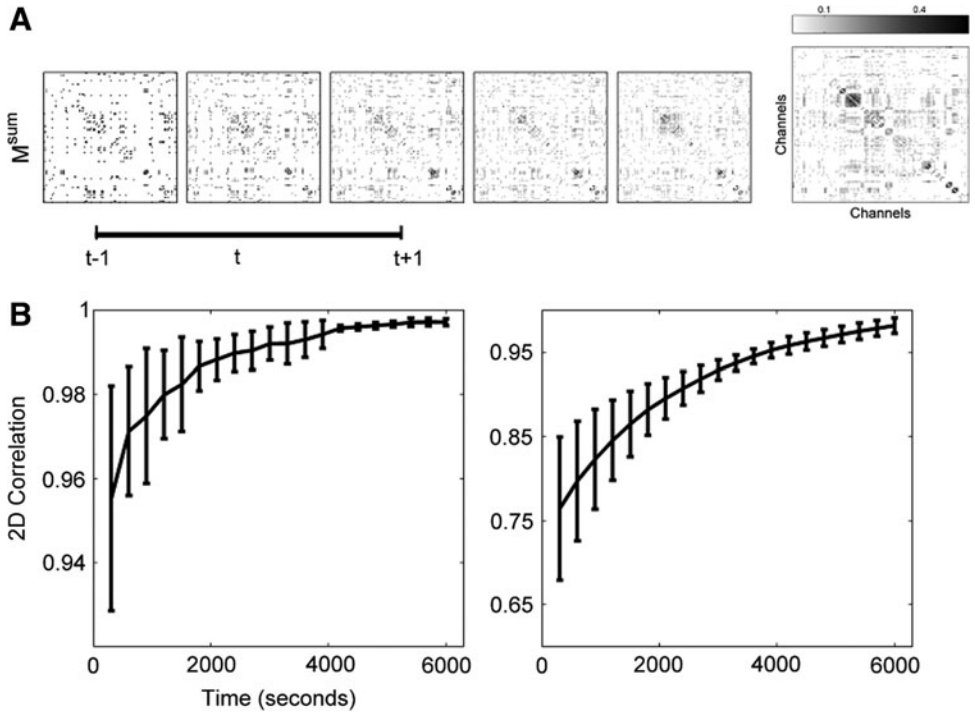

FIG. 5. The results of ISC, though variable over single time segments, approaches a stable clustering. **(A)** The cumulative sum of M is shown for five consecutive time segments (M_t^{sub} for $t = 1, \ldots, 5$). M^{sum}, the sum over the entire signal, is shown on the far right. The cumulative sum quickly begins to resemble the final configuration. **(B)** Left: Two-dimensional correlation between clustering results when the cumulative sum is compared with itself at two time points ($t-1$) and ($t+1$). The correlation between clustering results approaches 98% in about one half hour. This result pools values across all subjects, with standard error shown. Right: The cumulative sum of clustering results also becomes very similar to the final clustering, but more slowly. At 3600 sec, correlation between sub-clustering results and the final results is at 95% across all subjects (with standard error shown).

results from the various subsets of data resemble the clustering results using the entire signal very strongly, with a correlation of 95% (Fig. 5B).

In short, the ISC algorithm identifies clusters of electrodes corresponding to functional cortex, using correlations in infra-slow gamma band power fluctuations. This includes motor and visual cortex as determined using ECS, and putative DMN and attentional network cortex using anatomic location and the anti-correlated infra-slow fluctuations between these areas. While there appears to be heterogeneity within these clusters when time segments are viewed independently, the cumulative sum across time segments stabilizes quickly and allows our algorithm to produce reliable clustering results after about one half hour.

Discussion

Using a graph-based, spectral clustering algorithm and infra-slow co-fluctuations in HG BLP, we are able to reliably group electrodes into clusters that reflect functional organization of the brain. Inter-electrode correlations in HG power have shown clear selectivity for functional networks (Ko et al., 2011; Leopold et al., 2003; Nir et al., 2008), but these previous ECoG studies used *a priori* knowledge of cortical functional topography to select either regions of interest or "seed" electrodes for correlational comparisons. While others have used data-driven methods to map sensorimotor cortex using slow cortical potentials (Breshearset al., 2012), ISC is unique insofar as it examines HG power to classify electrodes into functionally relevant networks. In doing so, it avoids problems associated with clinical amplifiers that impose a high-pass filter on ECoG signal.

ISC correspondence with function

We present three lines of evidence suggesting a good correspondence between ISC clustering of infra-slow HG band responses and functionally connected networks. First and most importantly, identified clusters were consistent with the results from ECS mapping, the gold standard for functional mapping. Next, clusters detected by this algorithm are spatially distinct yet span significant distances—some clusters map to the corresponding cortex on the opposite hemisphere (Fig. 2B), and the attentional clusters anticorrelated with DMN clusters simultaneously cover distinct and distant areas of cortex such as the iPL and DLPFC (Fig. 3A). This implies that these clusters are not merely the result of local effects such as volume conduction. Finally, the DMN clusters identified by ISC exhibit HG modulations that are negatively correlated with electrodes overlying areas commensurate with dorsal and ventral attentional systems, a functional relationship consistent with fMRI studies (Fox et al., 2005, 2006).

These results have several implications. First, the high specificity of this algorithm may be useful in tailoring clinical functional mapping performed with ECS. In addition, the

anatomic locations and functional behavior of our clusters also provide support that infra-slow fluctuations in HG band power represent the neurophysiological basis of resting-state networks illuminated by rsfMRI BOLD fluctuations. Importantly, the identification of a functional relationship between clustered electrodes at this time scale has important implications for understanding the mechanisms contributing to how different regions of the brain interact during a resting state. Although rsfMRI assessments of fc do reveal dynamic patterns of connectivity, they rely on cerebrovascular changes that are correlated to neural activity resulting in the addition of confounding non-neural sources of noise. ECoG recordings, on the other hand, more precisely reflect the raw spontaneous activity of neuronal populations. Therefore, future ECoG efforts coupled with ISC will likely yield a greater understanding of the functional role and significance of spontaneous yet functionally organized neural activity.

Variations in cluster stability

ISC identifies sub-clusters of electrodes during time segments measured in hundreds of seconds, and repeats this over time; the final grouping of electrodes is based on the persistence of these sub-clusters across all time segments. Other approaches to the examination of functional networks over time also provide evidence of frequency-dependent network motifs, with core connections that appear frequently and concurrently, independent of transient activity. These template networks were also shown to be similar when measured on different days, implying that they are stable across very long time periods (Kramer et al., 2011). We not only find a similar persistence in fc over long periods of time, but also note that individual time segments can produce very different clustering results. In other words, we see significant correlations in infra-slow HG band activity that are transient, and others which are persistent. This may result from the lack of behavioral control during the clinical recordings we use; infra-slow modulation of gamma band power may change during differing behavioral contexts, thereby changing correlations between these signals. The rsfMRI literature suggests this may be the case, with scale-dependent temporal variability in network connectivity over time (Chang and Glover, 2010), and dynamic changes evident in measures of modularity corresponding to learning of motor tasks (Bassett et al., 2011). The heterogeneity in the persistence of these interactions is worthy of further investigation to determine whether this reflects shorter-lived connectivity that is random, context-related, or evidence of a more complex temporal structure which fluctuates on a separate time scale.

Limitations

This study does not compare rsfMRI and ECoG data; instead, it uses ECS as a surrogate for identifying the cortex involved in somatomotor functional networks. Examining co-fluctuations in infra-slow HG power concurrently with BOLD signal would be more ideal, but such data were not available.

There are discrepancies between cortical stimulus mapping and functional areas identified using spectral clustering. This may arise not only from inaccuracy of our method but also from several confounding factors. Our methods measure correlations of cortical fluctuations from beneath electrodes, while the bipolar stimulation used during cortical stimulation mapping involves the cortex between two electrodes, and as a result a one-to-one correspondence between the two techniques may not be precise. Moreover, the notion of "functional connectivity" as characterized by our algorithm, and functional status as determined by ECS, are fundamentally different insofar as fc is likely to indicate involvement in a particular functional system; while ECS identifies a cortex that, if disturbed, causes dysfunction in a particular functional system. This distinction is important, and may explain similar discrepancies in mapping when using other non-ECS modalities for identifying functional cortex (Breshears et al., 2012; Miller et al., 2011). Nevertheless, this technique has good specificity for identifying functionally relevant cortex, and mirrors functional relationships that are borne out by studies using other modalities.

Conclusions

This study shows successful data-driven identification of functional networks corresponding to motor, visual, and DMN cortex, using endogenous co-fluctuations in infra-slow HG power. Using measures of connectivity in spontaneous ECoG, ISC identifies clusters of electrodes overlying cortical fields with good specificity when compared with ECS, and clusters thus identified show some functional relationships consistent with fMRI studies of anti-correlated resting-state networks. Changes in connectivity measured by ISC over time may reflect interactions between networks as a function of behavioral or attentional state.

Acknowledgments

Research reported in this publication was supported by the National Institutes of Health under award numbers T32 NS 07144, 5K01 MH086118-03, and R01 NS065186. The content is solely the responsibility of the authors and does not necessarily represent the official views of the National Institutes of Health.

Author Disclosure Statement

No competing financial interests exist for the authors of this article.

References

Bassett DS, Wymbs NF, Porter MA, Mucha PJ, Carlson JM, Grafton ST. 2011. Dynamic reconfiguration of human brain networks during learning. Proc Natl Acad Sci USA 108: 7641–7646.

Bianciardi M, Fukunaga M, et al. 2009. Modulation of spontaneous fMRI activity in human visual cortex by behavioral state. Neuroimage 45:160–168.

Breshears JD, Gaona CM, et al. 2012. Mapping sensorimotor cortex with slow cortical potential resting-state networks while awake and under anesthesia. Neurosurgery 71:305–316.

Breshears JD, Roland JL, et al. 2010. Stable and dynamic cortical electrophysiology of induction and emergence with propofol anesthesia. Proc Natl Acad Sci USA 107:21170–21175.

Chang C, Glover G. 2010. Time–frequency dynamics of resting-state brain connectivity measured with fMRI. Neuroimage 50:81–98.

Crone NE, Miglioretti DL, et al. 1998. Functional mapping of human sensorimotor cortex with electrocorticographic spectral

analysis. II. Event-related synchronization in the gamma band. Brain 121:2301–2315.
Damoiseaux JS, Rombouts SA, et al. 2006. Consistent resting-state networks across healthy subjects. Proc Natl Acad Sci USA 103:13848–13853.
Deco G, Jirsa VK, et al. 2011. Emerging concepts for the dynamical organization of resting-state activity in the brain. Nat Rev Neurosci 12:43–56.
Fox MD, Corbetta M, et al. 2006. Spontaneous neuronal activity distinguishes human dorsal and ventral attention systems. Proc Natl Acad Sci USA 103:10046–10051.
Fox MD, Snyder AZ, et al. 2005. The human brain is intrinsically organized into dynamic, anticorrelated functional networks. Proc Natl Acad Sci USA 102:9673–9678.
He BJ, Snyder AZ, et al. 2008. Electrophysiological correlates of the brain's intrinsic large-scale functional architecture. Proc Natl Acad Sci USA 105:16039–16044.
Jerbi K, Ossandon T, et al. 2009. Task-related gamma-band dynamics from an intracerebral perspective: review and implications for surface EEG and MEG. Hum Brain Mapp 30: 1758–1771.
Kelly C, Biswal BB, et al. 2012. Characterizing variation in the functional connectome: promise and pitfalls. Trends Cogn Sci 16:181–188.
Ko AL, Darvas F, et al. 2011. Quasi-periodic fluctuations in default mode network electrophysiology. J Neurosci 31:11728–11732.
Kramer MA, Eden UT, et al. 2011. Emergence of persistent networks in long-term intracranial EEG recordings. J Neurosci 31:15757–15767.
Leopold DA, Logothetis NK. 2003. Spatial patterns of spontaneous local field activity in the monkey visual cortex. Rev Neurosci 14:195–205.
Leopold DA, Murayama Y, et al. 2003. Very slow activity fluctuations in monkey visual cortex: implications for functional brain imaging. Cereb Cortex 13:422–433.
Miller KJ, Abel TJ, et al. 2011. Rapid online language mapping with electrocorticography. J Neurosurg Pediatr 7: 482–490.
Miller KJ, Makeig S, et al. 2007. Cortical electrode localization from X-rays and simple mapping for electrocorticographic research: The Location on Cortex (LOC) package for MATLAB. J Neurosci Methods 162:303–308.
Miller KJ, Zanos S, et al. 2009. Decoupling the cortical power spectrum reveals real-time representation of individual finger movements in humans. J Neurosci 29:3132–3137.
Murias M, Swanson JM, et al. 2007. Functional connectivity of frontal cortex in healthy and ADHD children reflected in EEG coherence. Cereb Cortex 17:1788–1799.
Nir Y, Mukamel R, et al. 2008. Interhemispheric correlations of slow spontaneous neuronal fluctuations revealed in human sensory cortex. Nat Neurosci 11:1100–1108.
Papademetris X, Jackowski M, Rajeevan N, Okuda H, Constable RT, Staib LH. 2006. BioImage Suite: An integrated medical image analysis suite, Section of Bioimaging Sciences, Department of Diagnostic Radiology, Yale School of Medicine. www.bioimagesuite.org
Power JD, Barnes KA, et al. 2012. Spurious but systematic correlations in functional connectivity MRI networks arise from subject motion. Neuroimage 59:2142–2154.
Shi J, Malik J. 2000. Normalized cuts and image segmentation. IEEE Trans Pattern Anal Mach Intell 22:888–905.
von Luxburg U. 2007. A tutorial on spectral clustering. Stat Comput 17:395–416.
Zhang D, Johnston JM, et al. 2009. Preoperative sensorimotor mapping in brain tumor patients using spontaneous fluctuations in neuronal activity imaged with functional magnetic resonance imaging: initial experience. Neurosurgery 65:226–236.

Address correspondence to:
Andrew L. Ko
Department of Neurological Surgery
Oregon Health & Science University
Center for Health & Healing, CH8N
3303 SW Bond Avenue
Portland, OR 97239

E-mail: and@ohsu.edu